nature communications

Article

https://doi.org/10.1038/s41467-025-65033-2

Achieving high strain hardening and strength in an additively manufactured titanium alloy

Received: 4 December 2024

Accepted: 3 October 2025

Published online: 20 November 2025

Check for updates

Huizhi Peng[1,2], Yuman Zhu[1,2] ✉, Jun Wang[3,4], Jiaming Zhu[5,6], Jianwen Liu[1,2], Kai Zhang[1,7], Peter Lynch[3,4], Hamish L. Fraser[8], Peter Hodgson[3], Martin Heilmaier[9], Nick Birbilis[10], Yunzhi Wang[8] ✉ & Aijun Huang[1,2] ✉

Strain hardening is a crucial property of metals and alloys that directly affects their mechanical processability, safe usage, and durability throughout their service life. However, titanium alloys traditionally used in structural applications often exhibit limited strain hardening, restricting their broader use. In this work, we demonstrate that by employing additive manufacturing (AM), strong strain hardening with high strength can be simultaneously achieved in a commercially available titanium alloy. These remarkable properties arise from a martensitic microstructure originated from the AM process. The microstructure is characterized by nanosized martensite plates with extremely fine triple-twinned substructures. During tensile deformation, detwinning rather than dislocation slip gradually transforms this microstructure into single-twinned lamellae with ~10 nm twin boundary spacing and internal stacking faults, necessitating progressively higher stresses and resulting in significant strain hardening.

Strain hardening, also known as work hardening, is a fundamental strengthening mechanism by which metals can become stronger and more durable through plastic deformation. This phenomenon occurs when a metal undergoes deformation beyond its elastic limit, generating dislocations in the crystal structure which then interact with each other and multiply, increasing the material's hardness and strength[1,2]. The significance of strain hardening lies in its ability to enhance the capacity of a metallic component to resist fracture and failure during operational service[3], an essential quality for ensuring the safety and longevity of components and structures subjected to high stress and demanding load conditions. The principles of strain hardening date back to early metalworking, where artisans discovered that hammering could increase metal hardness—a concept that remains a cornerstone in modern industrial practices[4]. As a result, metals with excellent strain hardening properties, such as austenitic steels[5] and aluminum alloys[6], have found extensive applications and can be engineered to withstand stress environments approaching 65% of their yield strength or more[7]. These hardening processes are typically incorporated during alloy processing, well before a metal's service life begins. In contrast, some metals, including titanium alloys, demonstrate inadequate strain hardening[8] or are even susceptible to strain softening[9]. Despite their utilization in structural components across the aerospace and marine sectors because of their light weight and exceptional corrosion resistance, the limited strain hardening

[1]Monash Centre for Additive Manufacturing, Monash University, Melbourne, VIC, Australia. [2]Department of Materials Science and Engineering, Monash University, Melbourne, VIC, Australia. [3]Institute for Frontier Materials, Deakin University, Geelong, VIC, Australia. [4]Manufacturing Business Unit, Commonwealth Scientific and Industrial Research Organization (CSIRO), Melbourne, VIC, Australia. [5]School of Civil Engineering, Shandong University, Jinan, Shandong, China. [6]Shenzhen Research Institute, Shandong University, Shenzhen, Guangdong, China. [7]School of Materials Science and Engineering, University of Shanghai for Science and Technology, Shanghai, China. [8]Department of Materials Science and Engineering, Center for the Accelerated Maturation of Materials, The Ohio State University, Columbus, OH, USA. [9]Institute for Applied Materials (IAM-WK), Karlsruhe Institute of Technology (KIT), Karlsruhe, Germany. [10]Faculty of Science, Engineering, and Built Environment, Deakin University, Geelong, VIC, Australia.
✉e-mail: yuman.zhu@monash.edu; wang.363@osu.edu; aijun.huang@monash.edu

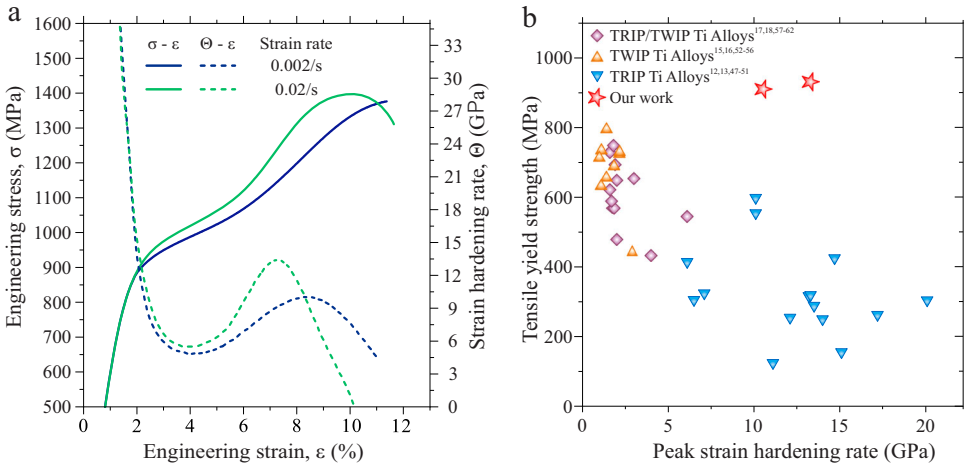

Fig. 1 | Tensile mechanical response of commercial Ti-6246 alloy produced by LPBF. a Engineering stress-strain curves and corresponding strain-hardening curves at strain rates of 0.002/s and 0.02/s. **b** Correlation of tensile yield strength and peak strain hardening rate of LPBF Ti-6246 titanium alloy and comparison with classic TRIP[12,13,47–51], TWIP[15,16,52–56], and TRIP/TWIP[17,18,57–62] titanium alloys.

capability confines them to stress environments below ~45% of their yield strength[7]. This restriction significantly impedes their application in advanced engineering fields where higher stress resistance is imperative.

The limited strain hardening ability of titanium alloys primarily originates from constrained dislocation storage within the close-packed hexagonal (HCP) α-phase[10], or restricted storage and enhanced dynamic recovery of dislocations within the body-centered cubic (BCC) β-phase[11] of the titanium matrix. Therefore, explorations of alternative pathways to accommodate plastic deformation and improve strain hardening are necessitated. In conventionally fabricated titanium alloys, two classical mechanisms, namely transformation-induced plasticity (TRIP) and twinning-induced plasticity (TWIP), have emerged as promising strategies to advance strain hardening. Specifically, the TRIP effect can provide substantial strain hardening, with peak strain hardening rates up to 20 GPa[12]. However, TRIP titanium alloys typically exhibit yield strengths under 600 MPa[13], which often does not meet the demands of many structural applications. The low yield strength is mainly due to the relatively low critical stress (190–370 MPa) required for the β-to-martensite (hexagonal α′ or orthorhombic α″) phase transformation[14]. In contrast, TWIP-enabled titanium alloys can achieve a relatively higher yield strength (up to 800 MPa[15]), but exhibit a much lower strain hardening rate (less than 3 GPa[16]). To achieve both excellent strain hardening and high yield strength, titanium alloys combining TRIP and TWIP mechanisms have also been developed. These TRIP + TWIP titanium alloys can reach a peak strain hardening rate up to 6 GPa[17] with a yield strength generally reaching 750 MPa[18]. However, this strength is still lower than that of the widely-used (workhorse) Ti-6Al-4V titanium alloy, which typically has a yield strength exceeding 900 MPa[8]. To date, it can be observed that higher yield strength and improved strain hardening in titanium alloys tend to be mutually exclusive. As such, reconciling this trade-off remains a significant challenge and an ongoing area of materials research[19,20]. Typically, titanium alloys featuring a heterogeneous microstructure composed of α phase, α′ martensite, and retained β phase have demonstrated enhanced strain hardening and strength due to the concurrent activation of reorientation-induced plasticity, TRIP, and TWIP mechanisms[21,22].

In the past decade, metal additive manufacturing (AM) has emerged as a highly flexible and efficient technology to fabricate intricate-geometry and near-net-shape titanium alloy parts, thereby also contributing to the expanded uptake of titanium alloys[23]. This evolution in manufacturing techniques has ignited significant interest in exploring the full potential of titanium alloys[24–28]. Among different AM technologies, laser powder bed fusion (LPBF) is particularly noteworthy for its rapid cooling rates, which foster the development of refined and LPBF-specific microstructures unattainable through traditional manufacturing methods.

In this work, we demonstrate that, by employing LPBF processing, a fully martensitic microstructure consisting of nanoscale martensite plates with internal triple-twinned substructure can be achieved in a commercial titanium alloy, i.e., Ti-6246 (Ti-6Al-2Sn-4Zr-6Mo, wt.%), which is commonly used in high-stress environments such as gas turbines and the oil and gas industry. Such martensitic microstructure enables a distinct deformation mechanism, offering a combination of superior strain hardening and high yield strength.

Results and discussion

Tensile properties

As shown in Fig. 1a, tensile tests were conducted on LPBF-fabricated Ti-6246 specimens along the AM build direction to evaluate their mechanical behavior under different strain rates (refer to "Methods" and Supplementary Information for alloy composition, preparation, and testing conditions). At a relatively low strain rate of 0.002/s, a high yield strength of 913 MPa was observed at room temperature; nearly twice that of conventionally fabricated and water-quenched counterparts (see Supplementary Fig. 1 and Supplementary Fig. 2) and comparable to that of double-annealed and forged ones (965 MPa)[8]. Upon further tensile deformation, the post-yield strength exhibits a dramatic increase, reaching approximately 1400 MPa at a uniform elongation of 11.3%. The nature of this increase in strength during deformation could be clearly identified from the changes in the corresponding strain hardening rate curve (Fig. 1a), which initially decreased after yielding to ~5 GPa at ~4% strain, then increased to a peak value of ~10.3 GPa at ~8% strain, before decreasing towards fracture. A similar secondary strain hardening behavior was also observed at a higher tensile strain rate of 0.02/s, albeit with a higher peak strain hardening rate of 13 GPa and a yield strength of 932 MPa. Notably, post-necking ductility also increased remarkably with strain rate, indicating strain-rate sensitivity in the post-necking regime. In comparison with traditional TRIP or TWIP titanium alloys, both stress-strain curves in Fig. 1a display markedly higher yield strengths while retaining superior strain hardening characteristics similar to those exhibited by TRIP titanium alloys that have a much lower strength, see the comparison in Fig. 1b. Hence, importantly this marks a significant departure from

https://doi.org/10.1038/s41467-025-65033-2

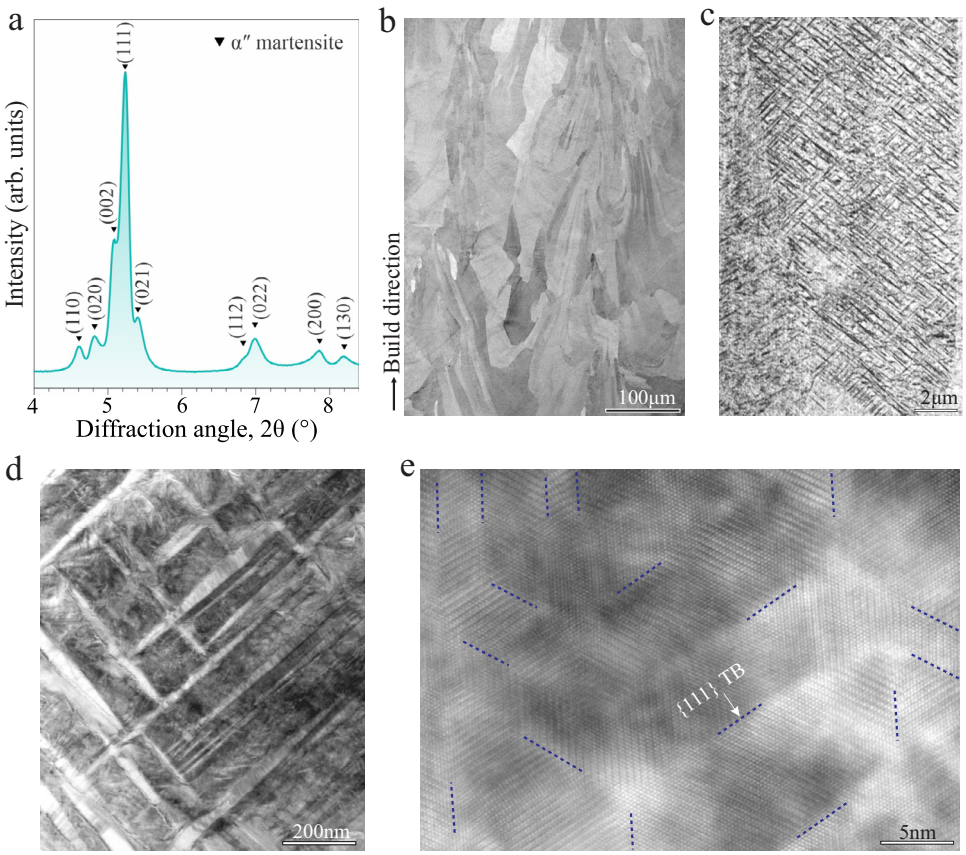

Fig. 2 | Characteristic martensitic microstructures in LPBF-produced Ti-6246 alloy. a T-SXRD spectrum revealing the α″ martensite phase in the as-built microstructure. **b** Low-magnification SEM image showing typical elongated prior-β grains aligned along the build direction shown by the black arrow. **c** High-magnification SEM image revealing dense basketweave α″ martensite plates within a prior-β grain. **d** Bright-field (BF) TEM image showing additional martensite variants apart from basketweave ones and other complex contrast. **e** High resolution TEM image showing triple twins within an individual martensite plate viewed along $<110>_{\alpha''}$. Three-oriented $\{111\}_{\alpha''}$ twin boundaries are indicated by blue dashed lines.

the conventional trade-off between yield strength and strain hardening inherent in titanium alloys.

As-built microstructure

To understand the origin of the unparalleled combination of high yield strength and strain hardening of AM-prepared Ti-6246, we conducted a comprehensive examination of the as-built microstructure. The transmission synchrotron X-ray diffraction (T-SXRD) spectrum (Fig. 2a) revealed only the presence of the α″ martensite phase (orthorhombic, with lattice parameters $a = 3.0517$ Å, $b = 4.9302$ Å, and $c = 4.6767$ Å) without any residual parent phase. Scanning electron microscopy (SEM) (Fig. 2b) showed the typical columnar-shaped prior-β grains aligned with the build direction. The prior-β grains consist of a distinctive basketweave microstructure (Fig. 2c), which was later revealed in Fig. 2d to be internally twinned α″ martensitic plates. A closer inspection of any individual α″ plate along its $<110>_{\alpha''}$ revealed an intriguing triple-twinned substructure—three martensite variants separated by three $\{111\}_{\alpha''}$ twin boundaries (TBs) (Fig. 2e and schematic in Supplementary Fig. 3; for crystallographic definitions of six α″ variants, please refer to Supplementary Note 1). The angle between every two TBs was approximately 120°, and the averaged spacing of the parallel TBs was ~7 nm (Supplementary Fig. 4), which even lies in the supra-nano range (1–10 nm)[29]. This martensitic microstructure originates from the complex thermal and mechanical cycles intrinsic to the LPBF process. To the best of our knowledge, the existence of such a fine triple-twinned structure in α″ martensitic plates has not been previously reported in conventionally fabricated counterparts and, thus, it is likely a feature resulting from the rapid cooling and complex thermal stress state inherent to the LPBF process.

Deformation mechanism

To further reveal the deformation mechanisms of this as-built microstructure, in-situ tensile T-SXRD was employed to monitor the entire tensile deformation process of the specimen at the lower strain rate of 0.002/s (see "Methods" and Supplementary Information for the experiment setup and data processing). The spectra for ten selected tensile strains shown in Fig. 3a consistently revealed the presence of only the α″ phase, with no indication of phase transformation across the imposed strain levels. This finding is consistent with the X-ray diffraction (XRD) results obtained with wider diffraction angles (refer to Supplementary Fig. 5). Although no phase transformation occurred during the tensile deformation, a detailed analysis of the in-situ tensile T-SXRD results indicated texture alterations of the α″ martensite as the tensile strain increased. As shown in the (100) pole figures in Fig. 3b, the texture intensities initially concentrated in the center and on the edge in the as-built condition, arising from six crystallographically equivalent α″ variants (two for the center and four for the edge). However, as the strain increased to around 8%, the texture intensities gradually reduced in the center, but increased at the edge. Beyond 8% strain, no further texture changes were observed. This texture evolution indicates a reduction in the number of α″ variants during tensile deformation (refer to Supplementary Note 2 for volume fraction of these variants over tensile strains retrieved from in-situ T-SXRD results).

https://doi.org/10.1038/s41467-025-65033-2

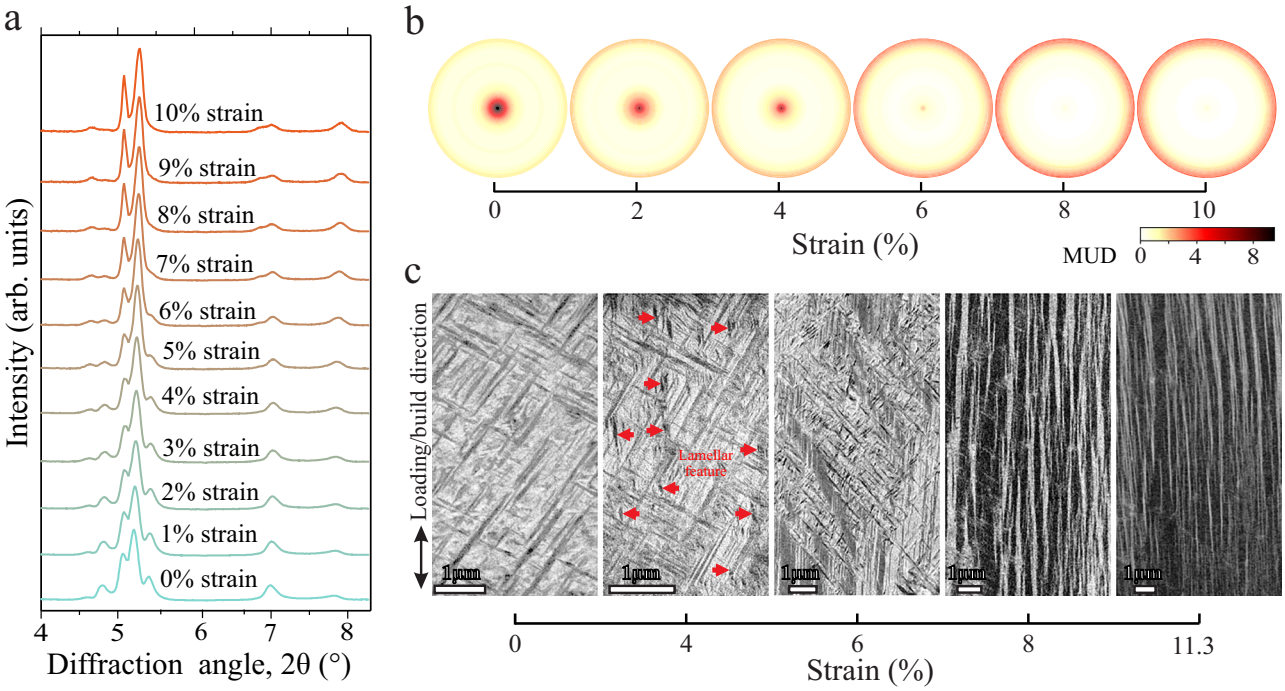

Fig. 3 | Microstructural evolution of the LPBF Ti-6246 sample during tensile deformation. a Selected in-situ T-SXRD spectra showing α″ martensite at eleven tensile strains from 0 to 10%. **b** Six representative (100) pole figures at different tensile strains retrieved from the in-situ T-SXRD showing the texture evolution of α″ martensite during tension. The out-of-page directions of pole figures are the build/loading directions. The legend shows the multiples of uniform distribution (MUD) values. **c** SEM images of interrupted tensile samples at different strains showing many lamellar-like features aligned along the build/loading direction that appear at 4% strain, as pointed out by red arrows, and grow with increasing strain. Scale bars, 1 μm.

The microstructural changes were further examined by SEM observations on tensile samples interrupted and unloaded at different tensile strains. As shown in Fig. 3c, compared to the fully basketweave martensitic microstructure within the prior-β grains of the as-built sample, newly formed lamellar-like features with a distinct darker contrast appeared in the 4% strained sample—with lengths less than 500 nm along the loading/build direction. As the tensile strain increased to 6%, these lamellae noticeably elongated and widened, with many having lengths exceeding 1 μm. At a strain of ~8%, elongated lamellae extended beyond 40 μm, occupying a significant portion of the microstructure until fracture occurred (see also Supplementary Fig. 6). It is noteworthy that such lamellar structure observed at approximately 8% strain correlates with the peak strain hardening rate (10.5 GPa), as illustrated in Fig. 1a. This underscores the significant strain-hardening ability inherent in the formation of the lamellar structure. Hence, it is clear that the triple-twinned structure evolves into a lamellar structure as plastic strain increases, and that it is this transformation that is responsible for the primary strain hardening. Subsequently, the gradually dominant lamellar structure continues to accommodate further tensile deformation with the formation of densely populated stacking faults (SFs) (see Fig. 4e), resulting in the secondary strain hardening behavior.

The lamellar-contrast areas that were observed in Fig. 3c from the 4% strained sample were further examined using transmission electron microscopy (TEM), where parallel lines with high density measuring less than 100 nm in length and 10 nm in spacing were observed (Fig. 4a). These lines were identified as edge-on $\{111\}_{\alpha''}$ TBs (Fig. 4b) and their orientations are identical to one of the three $\{111\}_{\alpha''}$ TBs observed within the triple-twinned substructure in the as-built microstructure (refer to Fig. 2e and Supplementary Fig. 7). Additionally, such TBs were all aligned closely with the loading direction (Fig. 4a). Interestingly, the other two $\{111\}_{\alpha''}$ TBs in the as-built microstructure, which were inclined to the loading direction, were not observed in this specific region. This observation suggests a detwinning process associated with these two TBs during deformation, accompanied by the disappearance of one variant among the initial three within the as-built martensite plates (Fig. 2e). This is consistent with the volume fraction decrease of certain α“ variants suggested by the texture evolution shown in Fig. 3b and Supplementary Note 2.

To provide further insight into the detailed detwinning process of the triple-twin structure, phase-field simulations were also carried out (Fig. 4c and Supplementary Fig. 8). To account for the stress environment during the AM process, a three-dimensional stress field obtained by multi-physics simulation for LPBF in the literature[30] was applied to the simulation cell. This residual stress led to the formation of a triple-twinned structure (see Fig. 4c), instead of the traditional herringbone structure typically observed in the absence of such stress. The simulated triple-twinned microstructure is in excellent agreement with the experimental observations (Fig. 2e). During tensile deformation, from the three twin-related martensite variants, one variant (the red-color variant in Fig. 4c) gradually shrinks under tensile strain. As a result, the TB that is more closely aligned with the loading direction remains and expands due to the growth of the other two retained variants (blue and tan variants), which is consistent with the experimental observations shown in Fig. 3c. Such a detwinning process driven by the external load to carry plastic strain (see Supplementary Fig. 9) becomes increasingly difficult. In other words, as the external load increases, the stress environment shifts from favoring three variants under residual stress to preferring two variants under tensile load, leading to the gradual shrinkage of the non-preferred variant. Thus, the interplays among the spatially non-uniform residual stress field, the uniform tensile load, and the local strain self-accommodation cause the detwinning process to occur under progressively higher external loads, contributing to significant strain hardening.

Further examination of the long lamellae in the as-fractured microstructure (Fig. 4d) confirmed the identical twin relationship

https://doi.org/10.1038/s41467-025-65033-2

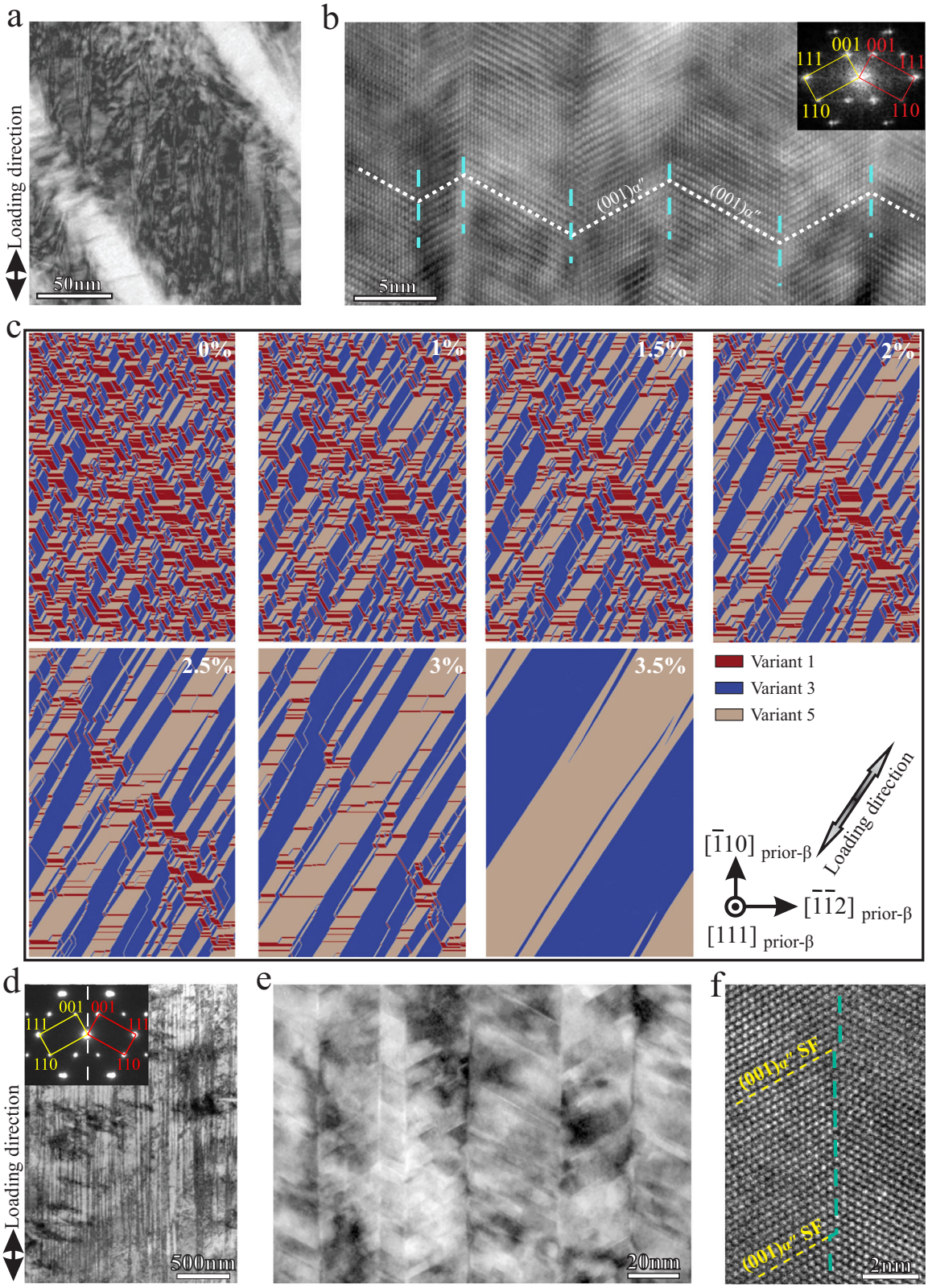

observed for the short lamellae (Fig. 4a, b). This is further supported by high-magnification TEM, as shown in Fig. 4e. The averaged TB spacing was measured to be around 10 nm in such regions. These lamellae, aligned parallel to the loading direction, have been previously associated with strain-rate sensitivity[31,32] and the higher post-necking ductility observed at higher strain rates (Fig. 1a), similar to behavior reported in nanotwinned copper[31]. Moreover, a high number density of $(001)_{\alpha''}$ SFs was observed within these regions, with most of them being interconnected with neighbouring TBs by a step having a single atomic layer of the TB plane in height, at intersection points (Fig. 4f and Supplementary Fig. 10). Such dense SFs within nanotwins have been previously suggested as a dominant component of secondary

Fig. 4 | Tensile strain-induced lamellae and their evolution with strain. a BF TEM image showing dense-packed parallel line contrast of lamellae at 4% strain. The viewing direction is parallel to $<110>_{\alpha''}$. Scale bar, 50 nm. **b** High resolution TEM image from (**a**) indicating that the parallel lines are $\{111\}_{\alpha''}$ TBs (shown by green dashed lines) separating two twin-related variants, confirmed by the corresponding Fast Fourier Transform (FFT) pattern inserted. Scale bar, 5 nm. **c** Phase-field simulation confirming that the triple martensite twins in the as-built microstructure undergo a detwinning process under tensile strain (values indicated at the upper-right corner of each image are transformation-induced strain along the loading direction), with two TBs reducing, leaving single-oriented twin lamellae aligned with the loading direction that expand until saturation. The martensite variants 1, 3, and 5 are expressed by red, tan, and blue colors. Tensile loading direction is along $[100]_{\beta}$. **d** BF TEM image of long lamellae in the as-fractured sample with inserted corresponding diffraction pattern revealing the $\{111\}_{\alpha''}$ twin relationship. Scale bar, 500 nm. **e** High-magnification TEM image of twin lamellae in (**d**) confirms the single-twinned martensite structure, similar to that shown in (**b**) and consistent with simulation results in (**c**). Additionally, dense $(001)_{\alpha''}$ SFs are notable within these twin-related variants (refer to Supplementary Fig. 8). Scale bar, 20 nm. **f** Atomic-resolution high-angle annular dark-field (HAADF) scanning transmission electron microscopy (STEM) image showing steps with a single-atomic-layer height of the TB plane at the intersection of SFs and TBs. The yellow and green dashed lines indicate SFs and TBs, respectively. Scale bar, 2 nm.

strain hardening and a consequence of deformation in nanotwinned materials[33]. Thus, it is reasonable to conclude that the dense SFs observed in this study play a critical role in the secondary strain-hardening behavior, further enhancing the material's resistance to deformation as strain increases.

In summary, by utilizing AM for the production of a commercial titanium alloy (Ti-6246), exceptional strain hardening with peak strain hardening rates over 10 GPa, together with high yield strengths exceeding 900 MPa, was achieved. The strong strain hardening observed at high yield strength was attributed to the martensitic microstructure generated by the LPBF process. This microstructure comprises nanoscale martensite plates with an internal triple-twinned substructure having an averaged TB spacing less than 10 nm, which significantly enhances the alloy's yield strength. During tensile deformation, the triple-twinned martensite structure underwent detwinning and transformed into single-oriented twin lamellae (averaged TB spacing around 10 nm) aligned along the loading direction, which is responsible for the primary strain hardening observed. Such close-packed twin lamellae also possess strong strain hardening ability by the formation of densely populated SFs within the individual martensitic domains of the lamellae, which is responsible for the notable secondary strain hardening of the alloy. These findings are expected to provide fundamental insights into strain hardening mechanisms in general while greatly expanding the application of titanium alloys in critical engineering structures.

Methods

Materials and fabrication

Commercial Ti-6246 powders produced by gas atomization were employed in this study. The composition of the alloy powders was analyzed using inductively coupled plasma-atomic emission spectroscopy conducted by Spectrometer Services Pty. Ltd. (VIC, Australia), and the details are presented in Supplementary Table 1. The majority of powder particles exhibit a nearly spherical morphology, as illustrated in Supplementary Fig. 11a. The particle size distribution of the alloy powders was determined by the laser diffraction technique using the Malvern Mastersizer 2000, revealing a size range of 14–100 µm in diameter with an average value of ~38 µm, as shown in Supplementary Fig. 11b.

The LPBF fabrication of Ti-6246 was performed in a commercial Concept Laser Xline 2000R equipped with Yb-fiber lasers. The printing parameters were optimized in this facility, resulting in the following settings: laser power of 370 W, spot size of 140 µm, hatch distance of 90 µm, scanning speed of 1600 mm/s, and layer thickness of 60 µm. During printing, a scanning path rotation of 67° (alternating) was applied to consecutive layers, and a protective argon atmosphere was maintained to ensure the oxygen level below 1000 ppm. The LPBF-fabricated samples exhibited a rod shape with a diameter of 10 mm and a height of 75 mm. Their relative density was determined to be ~99.9% based on analysis of over 25 optical microscopy images from the sample cross-section areas. Additionally, the chemical composition of the builds was verified to closely match the alloy powder (see Supplementary Table 1).

Mechanical testing

Tensile tests were conducted using an Instron 5892 machine at two different strain rates: 2×10^{-2}/s and 2×10^{-3}/s, following the ASTM E8/E8M standard. Before testing, the as-built rod samples were machined into a threaded cylindrical dog-bone shape with a gauge diameter of 4 mm and a gauge length of 20 mm. To ensure reproducibility, at least three tests were conducted for each strain rate condition. In addition, three interrupted tensile tests were carried out for the strain rate of 2×10^{-3}/s, with unloading at 4%, 6%, and 8% deformation strains, respectively.

X-ray diffraction

The XRD spectrum was recorded from the polished sample surface using a Bruker D8 Advance diffractometer with Cu K_{α} radiation (wavelength of 0.15406 nm) operated at 40 kV and 40 mA. The XRD scanning was conducted over the 2θ range of 30–90° at a step size of 0.05° and a dwell time of 50 s.

Scanning electron microscopy

SEM imaging of alloy powders was conducted using FEI Quanta 3D FEG-SEM operated at a working voltage of 10 kV and a current of 0.19 nA. For bulk samples, SEM imaging was performed in a Verios 5 UC FEG-SEM under the backscattered electron mode, operating at an acceleration voltage of 5 kV and a current of 0.8 nA. Prior to imaging, the samples were ion polished by the Gatan Precision Etching Coating System to eliminate any residual surface deformation. Subsequently, a 5-min plasma cleaning was applied using an XEI Scientific Evactron® 25 De-Contaminator equipment to minimize the carbon deposition during SEM scanning.

Transmission electron microscopy

Conventional TEM imaging was performed using an FEI Tecnai G^2 T20 TWIN TEM operating at 200 kV. The high-angle annular dark-field scanning transmission electron microscopy (HAADF-STEM) was conducted on a double C_s-corrected FEI Titan 80-300 at 300 kV with a selected convergence semi-angle of 15 mrad, providing a STEM resolution better than 0.12 nm. An inner collection semi-angle of approximately 64 mrad was set for the HAADF-STEM detector. For TEM sample preparation, 0.5 mm thick slices were first cut from the bulk samples or the gauge sections of tensile specimens parallel to the loading direction. Then, thin discs with a diameter of 3 mm were punched from these slices and ground to ~100 µm in thickness. After that, these discs were either twin-jet electropolished using the Struers Tenupol-5 system until a hole appeared in the center.

In-situ transmission synchrotron X-ray diffraction

The T-SXRD for in-situ tensile experiment was carried out on the imaging and medical beamline (IMBL)[34] of the Australian Synchrotron. The experimental setup is schematically shown in Supplementary Fig. 12. The dimension of the tensile specimen in the gauge part was 10 mm (length) × 2 mm (width) × 365 µm (thickness). The well-polished sample was installed on an in-situ tensile stage[35] with its thickness direction aligned to the beam direction. During deformation,

the tensile stage provided an increasing load with a rate of 11.4 N/s, leading to an average strain rate of ~0.002/s. A Canon EOS 550D camera was used to track the head displacement and obtain the applied strain by normalizing the displacement to the gauge length. A monochromatic X-ray beam with an energy of 60 keV and a beam size of 1.4 mm (width) × 1 mm (height) was used. A 2D detector was placed 960 mm behind the tensile sample to record diffraction patterns with a 1 Hz frequency. A beam stop was inserted between the sample and detector to block the center beam. Before the in-situ test, patterns from a LaB_6 standard sample (NIST Standard Reference Material SRM-660) were collected for calibration purposes.

The in-situ tensile T-SXRD results were first used for phase identification. The patterns collected before applying the tensile load were used to identify the phase in as-built samples. Specifically, the intensities were integrated along the azimuth angle (φ) from 3° to 357° (the azimuth angle was defined in Supplementary Fig. 10) to obtain the T-SXRD spectrum of the as-built sample. This spectrum was further analyzed in the GSAS-II software[36] to determine the lattice parameters. The patterns collected during the tensile deformation were used to continuously trace the phase under increasing strain. T-SXRD spectra at different strains were obtained by integrating intensities along the azimuth angle (φ) from 178° to 182° in the corresponding diffraction patterns.

The in-situ tensile T-SXRD results were further utilized for texture analysis. The diffraction patterns were segmented into cake pieces by a 1° azimuthal angle. In each cake, the intensities were integrated along the azimuthal angle to obtain the line profile. The line profiles were fitted by multiple PseudoVoigt functions to obtain the area for each peak. Here, the fiber-texture assumption[37,38] of prior-β grains was adopted along the loading/build direction[39]. Then, the pole figures for the (110), (020), (002), (111), and (021) planes were directly reconstructed. Based on these reconstructed pole figures, orientation distribution functions were estimated, and (100) pole figures were obtained using by Matlab toolbox MTEX[40].

Phase field modeling

The phase-field model is developed based on the combination of Landau theory[41], gradient thermodynamics[42], and Khachaturyan–Shatalov's microelasticity theory (KS-theory)[43]. The symmetry breaking accompanying the martensitic transformation from BCC to orthorhombic lattice structure leads to six crystallographically equivalent martensitic variants. Thus, the parent and martensitic phases are characterized by using six non-conserved structural order parameters, η_p ($p = 1$ - 6), with ($\eta_{p=1\sim6} = 0$) representing the parent phase and ($\eta_p = \pm1, \eta_{q=1\sim6,\, but q\neq p} = 0$) representing the pth correspondence variant of the martensitic phase. The total free energy functional, F, of the system is formulated as the following[44,45]

$$F = \int \left[\frac{1}{2}\kappa_\eta \sum_{p=1}^{6} \left(\nabla\eta_p\right)^2 + f_{ch}\left(\eta_1, \cdots \eta_6\right) + f_{ex}\left(\eta_1, \cdots \eta_6\right) \right] d^3\boldsymbol{r} + E_{el} \tag{1}$$

where $\kappa_\eta = 1.2 \times 10^{-12}$ J/m is the gradient energy coefficient for structural non-uniformities following the gradient thermodynamics, f_{ch} is the Landau free energy that describes the free energy of a local volume element having a uniform structural state characterized by $\eta_p(\mathbf{r})$ ($p = 1$–6), which can be approximated by the following polynomial

$$\begin{aligned} f_{ch}\left(\eta_1, \cdots \eta_6\right) = {} & \frac{1}{2}A_1(T - T_0)\sum_{p=1}^{6}\eta_p^2(\boldsymbol{r}) \\ & - \frac{1}{4}A_2\sum_{p=1}^{6}\eta_p^4(\boldsymbol{r}) + \frac{1}{6}A_3\left(\sum_{p=1}^{6}\eta_p^2(\boldsymbol{r})\right)^3 \end{aligned} \tag{2}$$

where $A_1 = 3.6 \times 10^5$ J/m³·K, $A_2 = 3.2 \times 10^7$ J/m³, $A_3 = 2.6 \times 10^7$ J/m³ are expansion coefficients[46]. The free energy associated with an external stress, σ_{kl}, is given by the following equation

$$f_{ex}\left(\eta_1, \cdots \eta_6\right) = -\sigma_{kl} \cdot \varepsilon_{kl}^{MT}(\boldsymbol{r}) \tag{3}$$

The E_{el} denotes the coherency elastic strain energy, which is calculated based on the KS-theory

$$E_{el} = \frac{1}{2}\sum_{p=1}^{6}\sum_{q=1}^{6}\int \frac{d^3k}{(2\pi)^3} B_{pq}(\boldsymbol{n})\left\{\eta_p^2\right\}_k \left\{\eta_q^2\right\}_k^* \tag{4}$$

where the integral is taken in the reciprocal space, $\boldsymbol{n} = \frac{\boldsymbol{k}}{k}$ is a unit vector, and $\boldsymbol{k}$ is a vector with modulus k in the reciprocal space, $\{\eta_p^2\}_k$ represents the Fourier transformation of η_p^2, $\{\eta_q^2\}_k^*$ is the complex conjugate of $\left\{\eta_q^2\right\}_k$.

$$B_{pq}(\boldsymbol{n}) = \begin{cases} C_{ijkl}\varepsilon_{ij}^{SF}(p)\varepsilon_{kl}^{SF}(q) & \boldsymbol{n} = 0 \\ C_{ijkl}\varepsilon_{ij}^{SF}(p)\varepsilon_{kl}^{SF}(q) - n_i\sigma_{ij}^0(p)\Omega_{jk}(\boldsymbol{n})\sigma_{kl}^0(q)n_l & \boldsymbol{n} \neq 0 \end{cases} \tag{5}$$

where $\sigma_{ij}^0(p) = C_{ijkl}\varepsilon_{kl}^{SF}(p)$, $\Omega_{ij}^{-1}(\boldsymbol{n}) = C_{iklj}n_k n_l$, and $\varepsilon_{kl}^{SF}(p)$ denotes the stress-free transformation strain of the pth martensitic variants, which are calculated from the following deformation matrices

$$\begin{aligned} \boldsymbol{U}_1 &= \begin{bmatrix} \zeta & 0 & 0 \\ 0 & \frac{\alpha+\gamma}{4} & \frac{\gamma-\alpha}{4} \\ 0 & \frac{\gamma-\alpha}{4} & \frac{\alpha+\gamma}{4} \end{bmatrix}, \boldsymbol{U}_2 = \begin{bmatrix} \zeta & 0 & 0 \\ 0 & \frac{\alpha+\gamma}{4} & \frac{\alpha-\gamma}{4} \\ 0 & \frac{\alpha-\gamma}{4} & \frac{\alpha+\gamma}{4} \end{bmatrix}, \boldsymbol{U}_3 = \begin{bmatrix} \frac{\alpha+\gamma}{4} & 0 & \frac{\gamma-\alpha}{4} \\ 0 & \zeta & 0 \\ \frac{\gamma-\alpha}{4} & 0 & \frac{\alpha+\gamma}{4} \end{bmatrix}, \\ \boldsymbol{U}_4 &= \begin{bmatrix} \frac{\alpha+\gamma}{4} & 0 & \frac{\alpha-\gamma}{4} \\ 0 & \zeta & 0 \\ \frac{\alpha-\gamma}{4} & 0 & \frac{\alpha+\gamma}{4} \end{bmatrix}, \boldsymbol{U}_5 = \begin{bmatrix} \frac{\alpha+\gamma}{4} & \frac{\gamma-\alpha}{4} & 0 \\ \frac{\gamma-\alpha}{4} & \frac{\alpha+\gamma}{4} & 0 \\ 0 & 0 & \zeta \end{bmatrix}, \boldsymbol{U}_6 = \begin{bmatrix} \frac{\alpha+\gamma}{4} & \frac{\alpha-\gamma}{4} & 0 \\ \frac{\alpha-\gamma}{4} & \frac{\alpha+\gamma}{4} & 0 \\ 0 & 0 & \zeta \end{bmatrix} \end{aligned} \tag{6}$$

where $\alpha = \sqrt{2}b/a_0$, $\zeta = a/a_0$, $\gamma = \sqrt{2}c/a_0$, with a_0, a, b, and c being the lattice parameters of the parent and martensitic phase. The following time-dependent Ginzburg-Landau equation is used to describe the temporal and spatial evolution of the structural order parameters during the MT

$$\frac{d\eta_p(\boldsymbol{r}, t)}{dt} = -M\frac{\delta F}{\delta\eta_p(\boldsymbol{r}, t)} + \xi_p(\boldsymbol{r}, t),\ p = 1 \sim 6 \tag{7}$$

where M is the kinetic coefficient and $\xi_p(\boldsymbol{r}, t)$ are the Langevin noise terms for structural fluctuations, which meets the following fluctuation-dissipation theorem:

$$\left\langle \xi_p(\boldsymbol{r}, t)\xi_p(r', t') \right\rangle = 2\frac{k_B T}{|\Delta f| l_0^3}\delta(\boldsymbol{r} - \boldsymbol{r}')\delta(t - t') \tag{8}$$

where k_B is the Boltzmann constant, T is the absolute temperature, $|\Delta f|$ is the chemical driving force (free energy difference between the parent and martensitic phases calculated from the Landau free energy), l_0 is the length scale assigned to the computational grid increment, and δ is the Kronecker delta function. Periodical boundary conditions are adopted in all three dimensions.

Data availability

Data supporting the findings of this study are provided within the manuscript and its associated Supplementary Information/Source data file. Source data are provided with this paper.

Code availability

The calculation methods used in this study are available within the manuscript and supplementary files.

References

1. Nabarro, F. R. & Duesbery, M. S. *Dislocations in Solids* (Elsevier, 2021).
2. Zepeda-Ruiz, L. A. et al. Atomistic insights into metal hardening. *Nat. Mater.* **20**, 315–320 (2020).
3. Antolovich, S. D. & Armstrong, R. W. Plastic strain localization in metals: origins and consequences. *Prog. Mater. Sci.* **59**, 1–160 (2014).
4. Meyers, M. A. & Chawla, K. K. *Mechanical Behavior of Materials* (Cambridge University Press, 2008).
5. Marshall, P. *Austenitic Stainless Steels: Microstructure and Mechanical Properties* (Elsevier Applied Science Publishers, 1984).
6. Lumley, R. *Fundamentals of Aluminium Metallurgy: Production, Processing and Applications* (Elsevier, 2010).
7. ASME. *ASME Boiler and Pressure Vessel Code: Section II—Materials* (American Society of Mechanical Engineers, 2021).
8. Welsch, G., Boyer, R. & Collings, E. *Materials Properties Handbook: Titanium Alloys* (ASM International, 1993).
9. Zhang, J. et al. Designing against phase and property heterogeneities in additively manufactured titanium alloys. *Nat. Commun.* **13**, 4660 (2022).
10. Argon, A. *Strengthening Mechanisms in Crystal Plasticity. Oxford Series on Materials Modelling*. Sutton, A. & Rudd, R. (Series Eds) (Oxford University Press, 2007).
11. Galindo-Nava, E. I. & Rivera-Díaz-del-Castillo, P. E. J. Modelling plastic deformation in BCC metals: dynamic recovery and cell formation effects. *Mater. Sci. Eng. A* **558**, 641–648 (2012).
12. Xiao, J., Shang, X., Hou, J., Li, Y. & He, B. Role of stress-induced martensite on damage behavior in a metastable titanium alloy. *Int. J. Plast.* **146**, 103103 (2021).
13. Ellyson, B. et al. Tuning the strength and ductility balance of a TRIP titanium alloy. *Scr. Mater.* **194**, 113641 (2021).
14. Ahmed, M., Wexler, D., Casillas, G., Savvakin, D. G. & Pereloma, E. V. Strain rate dependence of deformation-induced transformation and twinning in a metastable titanium alloy. *Acta Mater.* **104**, 190–200 (2016).
15. Zhang, J. et al. Strong and ductile beta Ti–18Zr–13Mo alloy with multimodal twinning. *Mater. Res. Lett.* **7**, 251–257 (2019).
16. Duport, M. et al. Processing, microstructures and mechanical response of a β-metastable Ti-14Mo alloy fabricated by Electron Beam Powder Bed Fusion. *Addit. Manuf.* **61**, 103340 (2023).
17. Fu, Y. et al. Ultrahigh strain hardening in a transformation-induced plasticity and twinning-induced plasticity titanium alloy. *Scr. Mater.* **187**, 285–290 (2020).
18. Sadeghpour, S. et al. A new multi-element beta titanium alloy with a high yield strength exhibiting transformation and twinning induced plasticity effects. *Scr. Mater.* **145**, 104–108 (2018).
19. Wu, X. et al. Heterogeneous lamella structure unites ultrafine-grain strength with coarse-grain ductility. *Proc. Natl. Acad. Sci. USA* **112**, 14501–14505 (2015).
20. Zhang, T. et al. In situ design of advanced titanium alloy with concentration modulations by additive manufacturing. *Science* **374**, 478–482 (2021).
21. Dumas, O., Malet, L., Kwaśniak, P., Prima, F. & Godet, S. Reorientation Induced Plasticity (RIP) in high-strength titanium alloys: an insight into the underlying mechanisms and resulting mechanical properties. *Acta Mater.* **246**, 118679 (2023).
22. Lee, S. W. et al. Reorientation-induced plasticity (RIP) in titanium alloys. *Acta Mater.* **275**, 120083 (2024).
23. Dutta, B. & Froes, F. H. *Additive Manufacturing of Titanium Alloys: State*. Hayton, J. (Plblisher), Gifford, C. (Acquisition Ed.), Cain, H. (Ed. Project Manager). (Butterworth-Heinemann, 2016).
24. Zhang, D. et al. Additive manufacturing of ultrafine-grained high-strength titanium alloys. *Nature* **576**, 91–95 (2019).
25. Zhu, Y. et al. Ultrastrong nanotwinned titanium alloys through additive manufacturing. *Nat. Mater.* **21**, 1258–1262 (2022).
26. Song, T. et al. Strong and ductile titanium–oxygen–iron alloys by additive manufacturing. *Nature* **618**, 63–68 (2023).
27. Qu, Z. et al. High fatigue resistance in a titanium alloy via near-void-free 3D printing. *Nature* **626**, 999–1004 (2024).
28. Zhang, J. et al. Ultrauniform, strong, and ductile 3D-printed titanium alloy through bifunctional alloy design. *Science* **383**, 639–645 (2024).
29. Sun, L. G., Wu, G., Wang, Q. & Lu, J. Nanostructural metallic materials: structure and mechanical properties. *Mater. Today* **38**, 114–135 (2020).
30. Wang, G. et al. The origin of high-density dislocations in additively manufactured metals. *Mater. Res. Lett.* **8**, 283–290 (2020).
31. You, Z. & Lu, L. Effect of strain rate on tensile ductility and fracture behavior of bulk nanotwinned copper. *Adv. Eng. Mater.* **17**, 1754–1759 (2015).
32. Lee, C., Youn, J. & Kim, Y. Effect of strain rate on the defect susceptibility of tensile properties to porosity variation. *Mater. Sci. Eng. A* **683**, 135–142 (2017).
33. Lu, L., You, Z. S. & Lu, K. Work hardening of polycrystalline Cu with nanoscale twins. *Scr. Mater.* **66**, 837–842 (2012).
34. Hausermann, D., Hall, C., Maksimenko, A. & Campbell, C. The imaging and medical beam line at the Australian synchrotron. *AIP Conf. Proc.* **1266**, 3–9 (2010).
35. Lynch, P. A. et al. A uniaxial tensile stage with tracking capabilities for micro X-ray diffraction applications. *J. Appl. Crystallogr.* **44**, 610–617 (2011).
36. Toby, B. H. & Von Dreele, R. B. GSAS-II: the genesis of a modern open-source all purpose crystallography software package. *J. Appl. Crystallogr.* **46**, 544–549 (2013).
37. Bian, X., Heller, L., Kadeřávek, L. & Šittner, P. In-situ synchrotron X-ray diffraction texture analysis of tensile deformation of nanocrystalline NiTi wire in martensite state. *Appl. Mater. Today* **26**, 101378 (2022).
38. Chen, Y. et al. Revealing the mode and strain of reversible twinning in B19′ martensite by in situ synchrotron X-ray diffraction. *Acta Mater.* **236**, 118131 (2022).
39. Liu, S. & Shin, Y. C. Additive manufacturing of Ti6Al4V alloy: a review. *Mater. Des.* **164**, 107552 (2019).
40. Hielscher, R. & Schaeben, H. A novel pole figure inversion method: specification of the MTEX algorithm. *J. Appl. Crystallogr.* **41**, 1024–1037 (2008).
41. Landau, L. D. & Lifshitz, E. M. *Statistical Physics* (Pergamon Press, 1980).
42. Cahn, J. W. & Hilliard, J. E. Free energy of a nonuniform system. I. Interfacial free energy. *J. Chem. Phys.* **28**, 258 (1958).
43. Khachaturyan, A. G. *Theory of Structural Transformations in Solids* (John Wiley & Sons, 1983).
44. Zhu, J., Gao, Y., Wang, D., Zhang, T.-Y. & Wang, Y. Taming martensitic transformation via concentration modulation at nanoscale. *Acta Mater.* **130**, 196–207 (2017).
45. Zhu, J. et al. Making metals linear super-elastic with ultralow modulus and nearly zero hysteresis. *Mater. Horiz.* **6**, 515–523 (2019).
46. Carrozza, A., Aversa, A., Fino, P. & Lombardi, M. Towards customized heat treatments and mechanical properties in the LPBF-processed Ti-6Al-2Sn-4Zr-6Mo alloy. *Mater. Des.* **215**, 110512 (2022).
47. Schaal, H., Castany, P. & Gloriant, T. Outstanding strain-hardening of a new metastable β-titanium alloy elaborated by in situ additive manufacturing L-PBF process. *Mater. Sci. Eng. A* **875**, 145117 (2023).
48. Maghsoudlou, A. et al. The room temperature tensile deformation behavior of thermomechanically processed β-metastable Ti-Nb-Ta-Zr bio-alloy: the role of deformation-induced martensite. *Mater. Sci. Eng. A* **738**, 15–23 (2018).

49. Cai, M.-H., Lee, C.-Y. & Lee, Y.-K. Effect of grain size on tensile properties of fine-grained metastable β titanium alloys fabricated by stress-induced martensite and its reverse transformations. *Scr. Mater.* **66**, 606–609 (2012).
50. Chong, Y., Gao, S. & Tsuji, N. A unique three-stage dependence of yielding behavior and strain-hardening ability in Ti-10V-2Fe-3Al alloy on phase fraction. *Mater. Sci. Eng. A* **821**, 141609 (2021).
51. Ma, X. et al. Effect of strain reversal on the stress-induced martensitic transformation and tensile properties of a metastable β titanium alloy. *J. Alloys Compd.* **784**, 111–116 (2019).
52. Ji, X., Emura, S., Min, X. & Tsuchiya, K. Strain-rate effect on work-hardening behavior in β-type Ti-10Mo-1Fe alloy with TWIP effect. *Mater. Sci. Eng. A* **707**, 701–707 (2017).
53. Xu, Y., Gao, J., Huang, Y. & Rainforth, W. M. A low-cost metastable beta Ti alloy with high elastic admissible strain and enhanced ductility for orthopaedic application. *J. Alloys Compd.* **835**, 155391 (2020).
54. Zhang, J. et al. Hierarchical {332}<113> twinning in a metastable β Ti-alloy showing tolerance to strain localization. *Mater. Res. Lett.* **8**, 247–253 (2020).
55. Lu, H. et al. Mechanical properties and deformation mechanism of a novel metastable β-type Ti–4V–2Mo–2Fe alloy. *Mater. Sci. Eng. A* **848**, 143376 (2022).
56. Huang, X., Li, J. & Lai, M. Influences of grain size on the deformation behavior of a twinning-induced plasticity metastable β titanium alloy. *J. Alloys Compd.* **937**, 168274 (2023).
57. Gao, J. et al. Deformation mechanisms in a metastable beta titanium twinning induced plasticity alloy with high yield strength and high strain hardening rate. *Acta Mater.* **152**, 301–314 (2018).
58. Sun, F. et al. Strengthening strategy for a ductile metastable β-titanium alloy using low-temperature aging. *Mater. Res. Lett.* **5**, 547–553 (2017).
59. Sun, F. et al. Investigation of early stage deformation mechanisms in a metastable β titanium alloy showing combined twinning-induced plasticity and transformation-induced plasticity effects. *Acta Mater.* **61**, 6406–6417 (2013).
60. Bortolan, C. C. et al. Effect of oxygen content on the mechanical properties and plastic deformation mechanisms in the TWIP/TRIP Ti–12Mo alloy. *Mater. Sci. Eng. A* **817**, 141346 (2021).
61. Zhu, C., Zhang, X. Y., Li, C., Liu, C. & Zhou, K. A strengthening strategy for metastable β titanium alloys: synergy effect of primary α phase and β phase stability. *Mater. Sci. Eng. A* **852**, 143736 (2022).
62. Zhang, J. et al. Fabrication and characterization of a novel β metastable Ti-Mo-Zr alloy with large ductility and improved yield strength. *Mater. Charact.* **139**, 421–427 (2018).

Acknowledgements

The authors wish to acknowledge the use of instruments and scientific and technical assistance at the Monash X-ray Platform (MXP), the Monash Centre for Nanofabrication (MCN) in the Victorian Node of the Australian National Fabrication Facility (ANFF), and the Monash Centre for Electron Microscopy (MCEM) as a Node of Microscopy Australia. The authors acknowledge some preliminary experimental trials using the lab X-ray beamline system at the InSitX Facility. InSitX is a joint program between Deakin University and Australia's Commonwealth Scientific and Industrial Research Organisation (CSIRO). The authors also want to thank the allocated beamtime (M20069) at the IMBL beamline of the Australian Synchrotron, part of ANSTO, and Dr Chris Hall for the technical support. The authors want to thank Dr. Kun Zhang and Dr. Xiang Gao for their support on preliminary microstructure characterizations. A.H., Y.Z., and P.H. thank the funding support from the Linkage Project (LP220100400) of the Australian Research Council (ARC). A.H., P.H., and Y.W. thank the funding support from the Discovery Project (DP250101360) of the Australian Research Council. Y.Z. acknowledges the funding support from the Future Fellow project (FT230100180) of the Australian Research Council. J.Z. thanks the support of the National Natural Science Foundation of China (No. 12372152), Shandong Provincial Natural Science Foundation (ZR2023MA058), and Guangdong Basic and Applied Basic Research Foundation (NO. 2023A1515011819). Y.W. acknowledges the U.S National Science Foundation (Grant No. DMR-2333551) that has facilitated this international collaboration.

Author contributions

A.H. and Y.Z. conceived the idea for this study. H.P., J.L., and K.Z. conducted the tensile tests. J.W., P.L., and H.P. performed the lab X-ray diffraction and in-situ transmission synchrotron X-ray diffraction. H.P. and Y.Z. conducted electron microscopy characterization. J.Z. and Y.W. carried out the phase-field simulations. H.P. and Y.Z. drafted the manuscript. All authors contributed to the discussion of the results and reviewing and editing the manuscript.

Competing interests

The authors declare no competing interests.

Additional information

Supplementary information The online version contains supplementary material available at https://doi.org/10.1038/s41467-025-65033-2.

Correspondence and requests for materials should be addressed to Yuman Zhu, Yunzhi Wang or Aijun Huang.

Peer review information *Nature Communications* thanks Indrani Sen and the other anonymous reviewer(s) for their contribution to the peer review of this work. A peer review file is available.